AAAS
Energy Material Advances
Volume 2021, Article ID 2712391, 11 pages
https://doi.org/10.34133/2021/2712391

Energy Material Advances
A SCIENCE PARTNER JOURNAL

Research Article

3-D Edge-Oriented Electrocatalytic $NiCo_2S_4$ Nanoflakes on Vertical Graphene for Li-S Batteries

Wenyue Li,[1] **Shiqi Li**,[2] **Ayrton A. Bernussi**,[3] **and Zhaoyang Fan**[1]

[1]*School of Electrical, Computer and Energy Engineering, Arizona State University, Tempe, Arizona, USA*
[2]*College of Electronic Information, Hangzhou Dianzi University, Hangzhou 310018, China*
[3]*Department of Electrical and Computer Engineering, Nano Tech Center, Texas Tech University, Lubbock, Texas, USA*

Correspondence should be addressed to Zhaoyang Fan; zhaoyang.fan@asu.edu

Received 18 December 2020; Accepted 25 February 2021; Published 22 March 2021

Polysulfide shuttle effect, causing extremely low Coulombic efficiency and cycling stability, is one of the toughest challenges hindering the development of practical lithium sulfur batteries (LSBs). Introducing catalytic nanostructures to stabilize the otherwise soluble polysulfides and promote their conversion to solids has been proved to be an effective strategy in attacking this problem, but the heavy mass of catalysts often results in a low specific energy of the whole electrode. Herein, by designing and synthesizing a free-standing edge-oriented $NiCo_2S_4$/vertical graphene functionalized carbon nanofiber (NCS/EOG/CNF) thin film as a catalytic overlayer incorporated in the sulfur cathode, the polysulfide shuttle effect is largely alleviated, revealed by the enhanced electrochemical performance measurements and the catalytic function demonstration. Different from other reports, the $NiCo_2S_4$ nanosheets synthesized here have a 3-D edge-oriented structure with fully exposed edges and easily accessible in-plane surfaces, thus providing a high density of active sites even with a small mass. The EOG/CNF scaffold further renders the high conductivity in the catalytic structure. Combined, this novel structure, with high sulfur loading and high sulfur fraction, leads to high-performance sulfur cathodes toward a practical LSB technology.

1. Introduction

In the Li-S battery (LSB) chemistry, *cyclo*-octasulfur (S_8), the most stable sulfur allotrope [1], undergoes a reduction process through multiple long-chain lithium polysulfide intermediates (Li_2S_x, $3 < x \leq 8$, or LiPSs) into Li_2S_2 and Li_2S. With this two-electron-based reaction per sulfur atom: $S_8 + 16\,Li^+ + 16\,e^- \leftrightarrow 8\,Li_2S$, the sulfur cathode can release a theoretical specific capacity of $1675\,mAh{\cdot}g^{-1}$, several folds higher than the transition-metal-oxide-based intercalation cathode materials. LSB has been regarded as a near-future technology that could deliver a specific energy of more than $350\,Wh{\cdot}kg^{-1}$, challenging the state of art of the Li-ion battery (LIB) technology. Owing to its earth abundance (17^{th} richest element), low production cost (~$200 per metric ton), and less toxicity, sulfur will also help reduce the battery cost and contribute to sustainable and environmentally benign battery technology development [2–4].

Developing a sulfur cathode technology, however, faces challenges of high resistivities of solid sulfur and Li_2S_2/Li_2S, a huge volume change between sulfur and Li_2S_2/Li_2S, and their sluggish redox reaction kinetics. Perhaps, the most formidable problem is the shuttle phenomenon of the soluble LiPSs and the subsequent adverse effects that cause low sulfur utilization, electrolyte depletion, lithium metal corrosion, and internal shortcut, resulting in low Coulombic efficiency and low cycling stability, among other issues [5–8].

Numerous methods have been investigated to address the polysulfide shuttle effect from different aspects in terms of sulfur host [9], binder [10], separator [11], and electrolyte [12]. Among those electrode engineering strategies, physically blocking the free diffusion of polysulfides by using a mesoporous conductive carbon host [13–15] or encapsulating sulfur in a hollow carbon sphere [16–18] has been widely reported. Chemically binding and stabilizing LiPSs on a polar host surface is more effective in reducing the shuttle effect. More strikingly, some binding surfaces act as catalysts, stabilizing the otherwise soluble LiPSs and accelerating the conversion between sulfur and Li_2S_2/Li_2S by decreasing their active energies. Doped carbon materials [19] and conductive

polymers [20], metal oxides [21, 22] and sulfides [23, 24], and single transition metal atoms [25] have all been theoretically and experimentally demonstrated with capability to stabilize LiPSs and catalyze their conversions. Among these catalytic candidates, metal sulfides are particularly interesting. Their versatile functionality in interacting with polysulfide, enhancing Li ion transportation, and controlling Li_2S precipitation gives them capability in curtailing the polysulfide shuttling process [26].

Admittedly, metal sulfides as a host material suffer from their low conductivity and large mass density when comparing to noncatalytic carbons. Clearly, organizing these two components together in a well-designed structure should provide a better solution [24, 27, 28]. Since catalytic function is a surface phenomenon, 2D sheet-like metal sulfides should be selected to minimize their mass loading, which if properly arranged on a conductive carbon scaffold will give an ideal host structure for the sulfur cathode. Although this conceptual design is straightforward, the studies along this approach are still very limited because of the difficulty in structure controlling.

Herein, we report well-dispersed $NiCo_2S_4$ ultrathin nanosheets as highly efficient catalyst, which were *in situ* grafted onto a vertical or edge-oriented graphene (EOG) scaffold [29, 30] to form an organized hierarchical structure used in sulfur cathodes. The EOG nanoflakes were grown around crosslinked carbon nanofibers (CNF), derived from electrospun polyacrylonitrile (PAN) nanofibers, producing a highly conductive, flexible, and freestanding EOG/CNF thin membrane. EOG nanoflakes mediated the nucleation and growth of $NiCo_2O_4$ (NCO) *via* the exposed active graphene edges [31], and NCO was subsequently sulfureted into $NiCo_2S_4$ (NCS) maintaining the 3-D edge-oriented sheet-like structure. To further minimize the mass loading of NCS in the electrode, instead of using a thick NCS/EOG/CNF layer as the sulfur host, a thin NCS/EOG/CNF catalytic layer was overlaid on the sulfur-loaded CNF membrane as a combined cathode to inhibit LiPSs shuttling. Here, we particularly avoid using the terminology of "interlayer" [32–34] to emphasize that this thin NCS/EOG/CNF catalytic overlayer is an integrated part of the cathode itself. This is because this conductive overlayer in the cathode, in addition to physically blocking LiPSs from shuttling which is the main function of a conventional interlayer [35], will chemically bind and catalytically promote the conversion of LiPSs to Li_2S_2/Li_2S or S_8 solids, which are the intrinsic function of the cathode itself. With the multiple unique features combined, this sulfur cathode structure exhibited attractive electrochemical performances of 1000 $mAh{\cdot}g^{-1}$ specific capacity at 0.3 C and 800 $mAh{\cdot}g^{-1}$ at 1 C within 400 cycles for 2 $mg{\cdot}cm^{-2}$ of sulfur loading and 850 $mAh{\cdot}g^{-1}$ specific capacity at 0.25 C for 6 $mg{\cdot}cm^{-2}$ of sulfur loading. An areal capacity of 4.5 $mAh{\cdot}cm^{-2}$ was demonstrated at the 100^{th} cycle under 0.3 C. By minimizing the "inactive" mass in the cathode, our design, with 6 $mg{\cdot}cm^{-2}$ sulfur loading, gives a sulfur fraction increase by 38.5% over a conventional design, translating to a significant increase in the possible specific energy based on the total cathode mass. Moreover, by virtue of the adaptability of the reported synthetic method and the prominent catalytic activity of the resulted product, this hierarchical structure can be further implemented in constructing other materials which are expected to deliver competitive electrochemical performances.

2. Experimental Section

2.1. Synthesizing Carbon Nanofiber Films. The carbon nanofiber film was fabricated by an electrospinning method. In a typical process, 0.5 g of PAN ($M_w = 150000\,g \cdot mol^{-1}$) was dissolved into 5 ml of dimethylformamide (DMF) and stirred at 80°C for 6 h. The PAN solution (1 ml) was ejected from a stainless-steel needle (inner diameter of 0.1 mm) attached to a 3 ml plastic syringe, which was driven at a rate of 1 $ml{\cdot}h^{-1}$ by a syringe pump. The electrospun PAN nanofiber film was collected on an aluminum foil. The electrostatic field was maintained at 1 $kV{\cdot}cm^{-1}$ between the needle and the collector. For carbonization, the PAN nanofiber film, after being peeled off from the Al foil, was first heated to 250°C at a rate of 2°C·min^{-1} and maintained at this temperature for 2 h to complete the preoxidation process. Then, the stabilized film was loaded into a tube furnace. With a temperature ramping rate of 2°C·min^{-1}, it was carbonized at 800°C for 2 h in nitrogen gas. The obtained freestanding carbon nanofiber film is designated as CNF. A thicker CNF, fabricated from 4 ml of PAN solution, was also prepared to serve as a freestanding cathode current collector and sulfur host for the sulfur cathode.

2.2. Synthesizing EOG-Modified CNF Films (EOG/CNF). EOG growth on CNF was implemented by a plasma-enhanced chemical vapor deposition (PECVD) technique. Briefly, the CNF film was loaded onto a molybdenum holder and placed into the plasma chamber which was pumped down to 10^{-4} torr. 50 sccm of CH_4 and 100 sccm of H_2 were introduced into the chamber to maintain the pressure at 30 torr. With the sample holder temperature reaching to 750°C, plasma was ignited with an input power of 1 kW. The EOG growth process lasted for 5 min.

2.3. Synthesizing $NiCo_2S_4$ Nanosheet-Modified EOG/CNF Films (NCS/EOG/CNF). The obtained EOG/CNF film was pretreated in a concentrated nitric acid at 80°C for 6 h to improve its hydrophilic property. After being washed in DI water and dried in an oven, the film was immersed into 20 ml solution comprised of 10 mM cobalt nitrate ($Co(NO_3)_2{\cdot}6H_2O$), 5 mM nickel nitrate ($Ni(NO_3)_2{\cdot}6H_2O$), and 2.5 mM urea in DI water and then sealed into an autoclave and heated for 16 h. Several temperatures were tested to optimize the structure of NCO grown on the EOG/CNF (Figure S1 in Supporting Materials (SI)). After this hydrothermal process, NCO nanosheets were grown on the EOG/CNF and the sample is designated as NCO/EOG/CNF. This film was further treated in Na_2S DI water solution (0.02 M) by hydrothermal method at 160°C for 6 h. During this step, $NiCo_2O_4$ was sulfureted into $NiCo_2S_4$ nanosheets and the resulted thin-film product is named as NCS/EOG/CNF.

2.4. Material Characterization. The morphology of the synthesized structures was characterized using a field emission

scanning electron microscopy (FE-SEM) (SUPRA35, Gemini) and a transmission electron microscopy (TEM) (H-8100, Hitachi). The crystalline features of the samples were studied *via* powder X-ray diffraction (XRD) (MiniFlex 6G, Rigaku), measured with 2θ from 10° to 80° using Cu Kα radiation. The surface chemical status and chemical bond information of different elements were investigated using an X-ray photoelectron spectroscopy (XPS) (5000 VersaProbe, PHI). UV-Vis-IR absorption spectroscopy analysis (Shimadzu UV-3600) was performed to evaluate the polysulfide adsorption capability of the prepared NCS/EOG/CNF thin film.

2.5. Electrochemical Measurement. Coin cells (CR2400) were assembled for electrode characterization. A blank electrolyte was prepared by dissolving an appropriate amount of lithium trifluoromethanesulfonate ($LiCF_3SO_3$) (1 M) and lithium nitrate ($LiNO_3$) (0.1 M) in 1,2-dimethoxyethane (DME) and 1,3-dioxolane (DOL) solution (1 : 1 by volume). Sublimed sulfur and lithium sulfide (Li_2S) were proportionally added into the blank electrolyte to form Li_2S_6 (1 M) catholyte. The CNF film (thickness ~30 μm), as cut into ~12 mm disks, was used as the current collector, and 12–36 μl of Li_2S_6 solution catholyte was added into the CNF disks to obtain 2–6 mg·cm^{-2} sulfur loading. The NCS/EOG/CNF film (~7 μm) was then laid on the top of the CNF disk followed by adding 10 μl of blank electrolyte. After placing the Celgard 2400 separator, another 10 μl of blank electrolyte was added, followed by a lithium metal disk as the anode. The whole stack was sealed into a coin cell and set for 6 h before the electrochemical measurements.

The cyclic voltammetry (CV) was measured at 0.1 mV·s^{-1} in a voltage range of 1.7–2.8 V. The electrochemical impedance spectroscopy (EIS) study was performed in 0.1–100 kHz with an AC voltage amplitude of 5 mV. Both measurements were conducted on an electrochemical workstation (Bio-Logic SP-150) with the sulfur cathode as the working electrode and the lithium metal as both the anode and the reference electrode. The battery galvanostatic charge-discharge characterizations were carried out using a battery tester (LANHE, CT2001A). For comparison, cells without and with other overlayers were also assembled and tested. These cells are called as CNF cell, EOG/CNF cell, NCS/CNF cell, NCO/EOG/CNF cell, or NCS/EOG/CNF cell.

3. Results and Discussion

3.1. Structural and Morphological Features of $NiCo_2S_4$ on the EOG/CNF Substrate. Figure 1(a) schematically illustrates the NCS/EOG/CNF film preparation process. The morphology of the sample at each step is presented by its scanning electron microscopy (SEM) images (Figures 1(b)–1(e)). The CNF film derived from electrospun PAN nanofibers was employed as a scaffold, offering flexibility and conductivity to the whole structure of NCS/EGO/CNF. Carbon nanofibers show an intertwined feature with a diameter from tens to around 200 nm. *Via* PECVD deposition, EOG nanoflakes were uniformly grown on the surface of an individual nanofiber. After treating the attained EOG/CNF in a concentrated nitric acid, oxygen functional groups were introduced onto the edge (Figure S2) and other defective sites of graphene nanoflakes, giving rise to an improved hydrophilic property (Figure S3). These active sites, in the subsequent hydrothermal synthesis process, promoted the absorption of the reactive ions and the nucleation of NCO. The morphological evolution of NCO on EOG was revealed by using *ex situ* SEM to monitor the intermediates at different reaction stages, the edge-oriented feature of the nanoflakes is maintained all through the growth process (Figure S4). In contrast, without the acid treatment, only large NCO nanoflakes were found on the surface of EOG/CNF (Figure S5). As shown in Figure 1(d), the NCO-modified CNF/EOG film preserves its vertical nanoscale feature, confirming that EOG nanoflakes serve as a structure mediator to control the oriented growth of NCO nanosheets. A subsequent sulfurization process transforms NCO nanosheets into NCS nanosheets while maintaining their vertical orientation (the NCS/CNF film was also prepared for comparison, as shown in Figure S6). The thickness of the whole NCS/EOG/CNF overlayer used here is around 7 μm (Figure S7). It should be noted that although NCS nanosheets can be grown onto CNF *via* a facile hydrothermal process, their size and thickness are much larger than the NCS obtained here by employing EOG as a growth mediator. The presented NCS/EOG/CNF structure can efficiently decrease the percentage of the catalyst and the mass of the whole layer without compromising their catalytic activity and polysulfide blocking ability.

Transmission electron microscopy (TEM) images (Figures 1(f)–1(h) and Figure S8) further reveal the microstructural features of these samples. The graphene thin nanoflakes, vertically grown on the nanofiber are clearly shown in Figure 1(f) and S8a. A high-resolution TEM image in Figure S8b confirms the lattice spacing of around 0.37 nm, in accordance with the (002) crystalline plane of graphite [36]. Due to the atomic mass difference of elements, the contrast changes in TEM images after NCO and NCS modification are revealed in Figures 1(g) and 1(h). Importantly, the vertical profile of nanoflakes is retained, visually proving the effectiveness of the structural regulation function of these EOG (Figure S8c, d). X-ray diffraction (XRD) patterns of different samples are presented in Figure 1(i). In comparison with the CNF film, whose characteristic peak locates at 2θ ~24° which belongs to the (002) crystalline plane of carbon, this graphite peak in other samples shifts to higher 2θ at around 26° with a sharper shape, indicating their improved graphitization degree due to the EOG deposition [37]. In addition, the other diffraction peak of graphite recorded at ~44° also emerges in the EOG samples and can be assigned to the graphite (101) crystalline plane. The appearance of peaks at 2θ ~16°, 31°, 38°, 50°, and 55° in the XRD pattern of NCS/EOG/CNF are in line with the (111), (311), (400), (511), and (440) diffraction patterns of the cubic phase NCS [38], which is converted from cubic-structured NCO after the sulfurization hydrothermal process [39]. To investigate the surface chemical status of the samples, X-ray photoelectron spectroscopy (XPS) was carried out and the

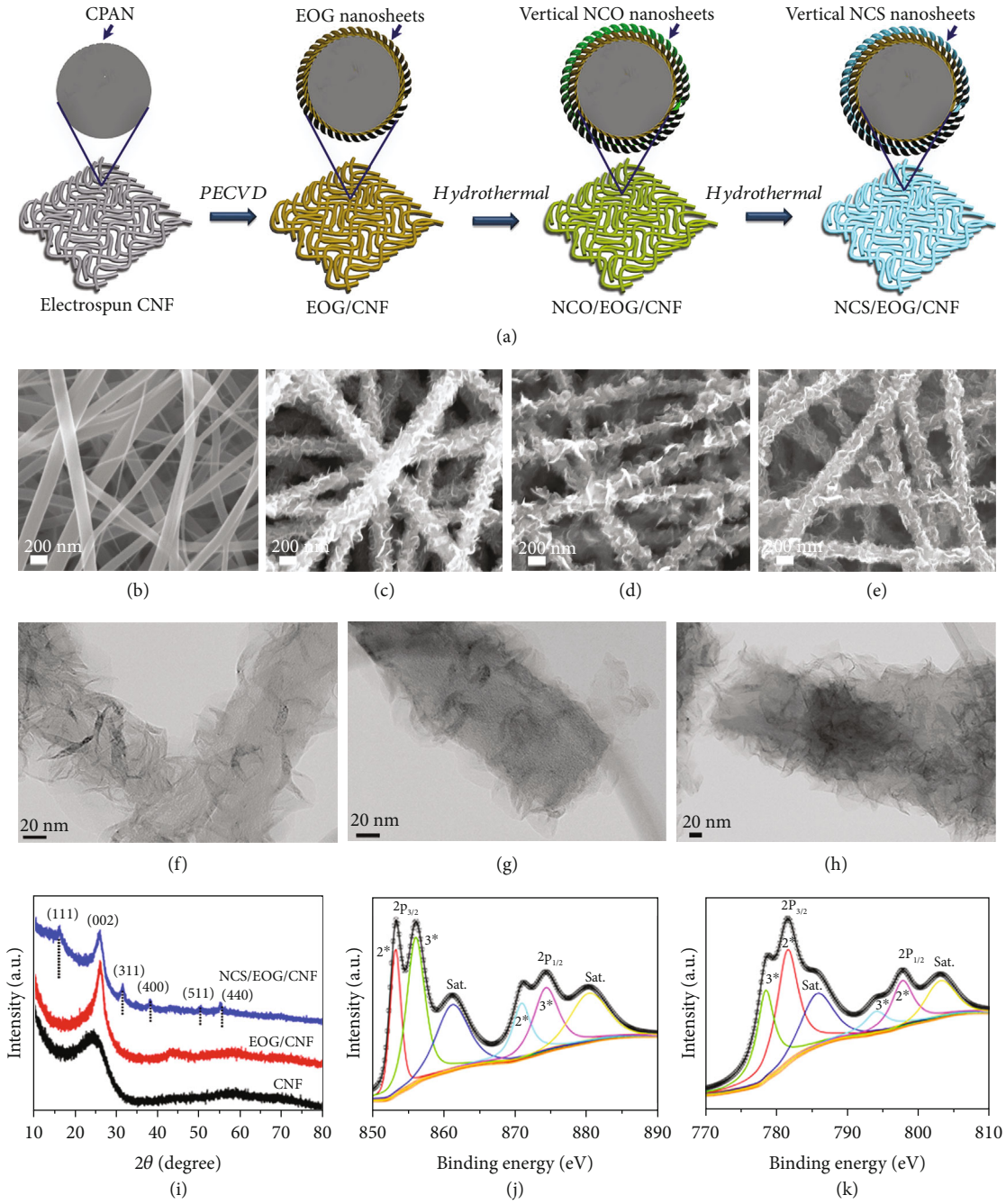

Figure 1: (a) Schematic illustration of NCS/VOG/CNF film preparation. SEM images of (b) CNF, (c) EOG/CNF, (d) NCO/EOG/CNF, and (e) NCS/EOG/CNF. TEM images of (f) CNF/EOG, (g) NCO/EOG/CNF, and (h) NCS/EOG/CNF. (i) XRD patterns of different samples. High-resolution XPS spectrum of (j) Ni 2p and (k) Co 2p peaks from the NCS/EOG/CNF sample.

results of their survey scan spectra are given in Figure S9, which indicates the presence of Ni, Co, and S elements in the NCS/EOG/CNF sample. The Ni 2p and Co 2p tight spectra were fitted with two spin-orbit doublets and two shakeup satellites by using a Gaussian fitting method. For Ni 2p (Figure 1(j)), the peaks located at 853.1 eV in Ni $2p_{3/2}$ and 871.3 eV in Ni $2P_{1/2}$ along with two satellites can be assigned to Ni^{2+}, while others centered at 856.1 and 873.9 eV are attributed to Ni^{3+}. Accordingly, with regard to the Co 2p, the characteristic peaks of Co^{3+} and Co^{2+} are emerged at 778.2/794.0 eV and 781.4/797.3 eV, respectively. The shakeup satellite peaks at 785.0 and 803.1 eV further confirm the coexistence of Co^{2+} and Co^{3+} statuses (Figure 1(k)). In addition, the fitting result of S 2p signal shown in Figure S10 gives more information of the existence of Co-S and Ni-S binding. Hence, these results demonstrate that the surface chemical components of the NCS/EOG/CNF film include Co^{2+}/Co^{3+}, Ni^{2+}/Ni^{3+}, and S^{2-}, which is consistent with other reported NCS materials [32, 40].

3.2. The NCS/EOG/CNF Overlayer as a Polysulfide Absorbent and Polysulfide Conversion Accelerator. To verify the catalytic function of the NCS/EOG/CNF layer in promoting the sulfur electrode performance, LSB cells assembled with different overlayers in the cathode were first studied using the cyclic voltammetry (CV) technique (Figure 2(a)). All the cells show two reductive peaks emerging at 2.30 and 2.05 V, contributed to the stepwise reduction of sulfur species to smaller polysulfide molecule and insoluble Li_2S [41]. Correspondingly, two oxidation peaks located at 2.32 and 2.40 V are originated from the reverse reactions of Li_2S converted back to S_8 [42]. Compared with the cell without an extra overlayer, the peaks of EOG/CNF, NCO/EOG/CNF, and NCS/EOG/CNF cells have a more defined shape and higher peak current densities. In addition, the peak differences (ΔE_p) between the corresponding oxidation and reduction reactions are also slightly reduced (e.g., ΔE_p between peak two and peak three of NCS/EOG/CNF cell decreases to 360 mV in comparison with 368 mV of EOG/CNF cell). These observations suggest that the catalytic overlayers, particularly NCS/EOG/CNF, can provide better reactive reversibility to polysulfide conversions [43]. In order to confirm the stability of the NCS within the scanning potential window, NCS/EOG/CNF cell with blank electrolyte was also measured using the CV technique under the same testing conditions. As shown in Figure S11, no redox peaks appeared in the potential range of 1.6–2.8 V, demonstrating that all the peaks originated from LiPSs conversion processes and the stability of NCS in the operative voltage window of LSB.

To evaluate the chemical binding ability of different materials to the soluble LiPSs, Li_2S_6 absorption by the pure CNF and the CNF with an EOG/CNF, NCO/EOG/CNF, or NCS/EOG/CNF overlayer was measured in 20 mM Li_2S_6 electrolyte. After soaking them in the same amount of electrolyte for about 1 hour, the strongest absorption of the NCS/EOG/CNF overlayer to Li_2S_6 can be visually observed *via* the electrolyte color change (Figure 2(b), inset). This is further quantified by the UV-Vis absorption spectroscopy of the electrolyte after soaking. As shown in Figure 2(b), the UV absorptance of the Li_2S_6 solution is greatly reduced after being soaked by the NCS/EOG/CNF layer, indicating that the Li_2S_6 concentration is much diminished due to the strong absorption by NCS. NCO/EOG/CNF and EOG/CNF layers also enhance polysulfide absorption, although at weakened extents. The chemical status of NCS after Li_2S_6 absorption experiment was further analyzed by XPS technique with the high-resolution spectrum of Ni 2p, Co 2p, and S 2p presented in Figure 2(c) and S12. In comparison with those of the pristine NCS overlayer, the Ni $2p_{3/2}$ and Co $2p_{3/2}$ peaks of the treated NCS shift to much lower binding energy, implying the occurrence of electron transfer from Li_2S_6 to the Ni and Co elements [44, 45]. In order to prove that this functionalized overlayer not only physically absorbs the polysulfide species but also actively participates their redox reactions, symmetric cells based on NCS/EOG/CNF or EOG/CNF electrodes were assembled with Li_2S_6 electrolyte and tested by using the CV technique within a potential window of −1.0 to 1.0 V. As exhibited in Figure S13, the redox peak current of Li_2S_6 in the NCS/EOG/CNF cell under the scan rate of 10 mV·s^{-1} is much larger than that in the EOG/CNF cell. Furthermore, with the scan rate increasing to 100 mV·s^{-1}, the CV curves of NCS/EOG/CNF cell show a more defined shape with smaller peak potential difference in comparison with those of EOG/CNF cell, indicating that the NCS part greatly facilitates the polysulfide reactions.

Electrochemical impendence spectroscopy (EIS) was applied to probe the function of a catalytic overlayer in the LSB cells. The EIS spectra of fresh cells were presented in Figure 2(d). All the spectra are comprised of two semicircles and an inclined line [46, 47], which can be modeled by the equivalent circuit in Figure 2(d), where R_1 represents the combined internal ohmic resistance of the electrolyte, separator, and electrode interfaces, R_2 represents the parallel resistance of an insulative SEI layer, R_3 represents the charge transfer resistance of LiPS conversions, CPE is a constant phase element, and W_o is the Warburg impedance. In the spectra, the first semicircle in the high-frequency range can be interpreted as the response from the insulative SEI layer. The other semicircle in the medium-frequency range can be modeled by the charge transfer process or the reduction reaction kinetics in the sulfur cathode. The linear part at low frequencies represents the ion diffusion within the cathode. As confirmed in Figure 2(e) which compares the fitted three resistive parameters, the four cells exhibit the very similar R_1 but the NCS/EOG/CNF cell has the smallest SEI resistance R_2 and charge transfer resistance R_3. The smallest R_3 signifies the strongest catalytic function of the NCS/EOG/CNF overlayer in the cathode and the smaller R_2 suggests that this overlayer also somehow reduced the thickness of the formed SEI layer, which is conducive to the cell rate performance.

To further probe the catalytic effect of NCS nanosheets on the redox kinetics of soluble polysulfides, CVs under different scan rates of 0.1–0.5 V·s^{-1} were acquired for cells with and without the NCS/EOG/CNF overlayer (Figure 2(f) and Figure S14). The current density of redox peaks was plotted against the square root of scan rates and revealed a linear relationship between them (Figure 2(g)), suggesting that the redox reaction rates are determined by the ion diffusion process. Their relationship can be interpreted by the following Randles-Sevcik equation [48]:

$$I_p = 2.69 \times 10^5 n^{1.5} D^{0.5} C v^{0.5} \quad (1)$$

where I_p is the peak current density, n is the charge transfer number, D is the ion diffusion coefficient of Li^+, C is the concentration of the polysulfide, and v is the scan rate. Since the LSBs are tested using the same configuration and the same amount of electrolyte, the n and C values in each reaction can be considered as constant and the slope can be used to represent the diffusivity of Li ions (D_{Li+}). In the LSB scenario, D_{Li+} includes the diffusion of Li^+ in the solution to the cathode surface and the quasisolid-state/solid-state diffusion in the LiPS formed on the sulfur surface. From the slops of the plots in Figure 2(g), the ratio of diffusion coefficients for every redox peak between the cell with the NCS/EOG/CNF overlayer and the cell without an overlayer in the cathode is summarized in Figure S15.

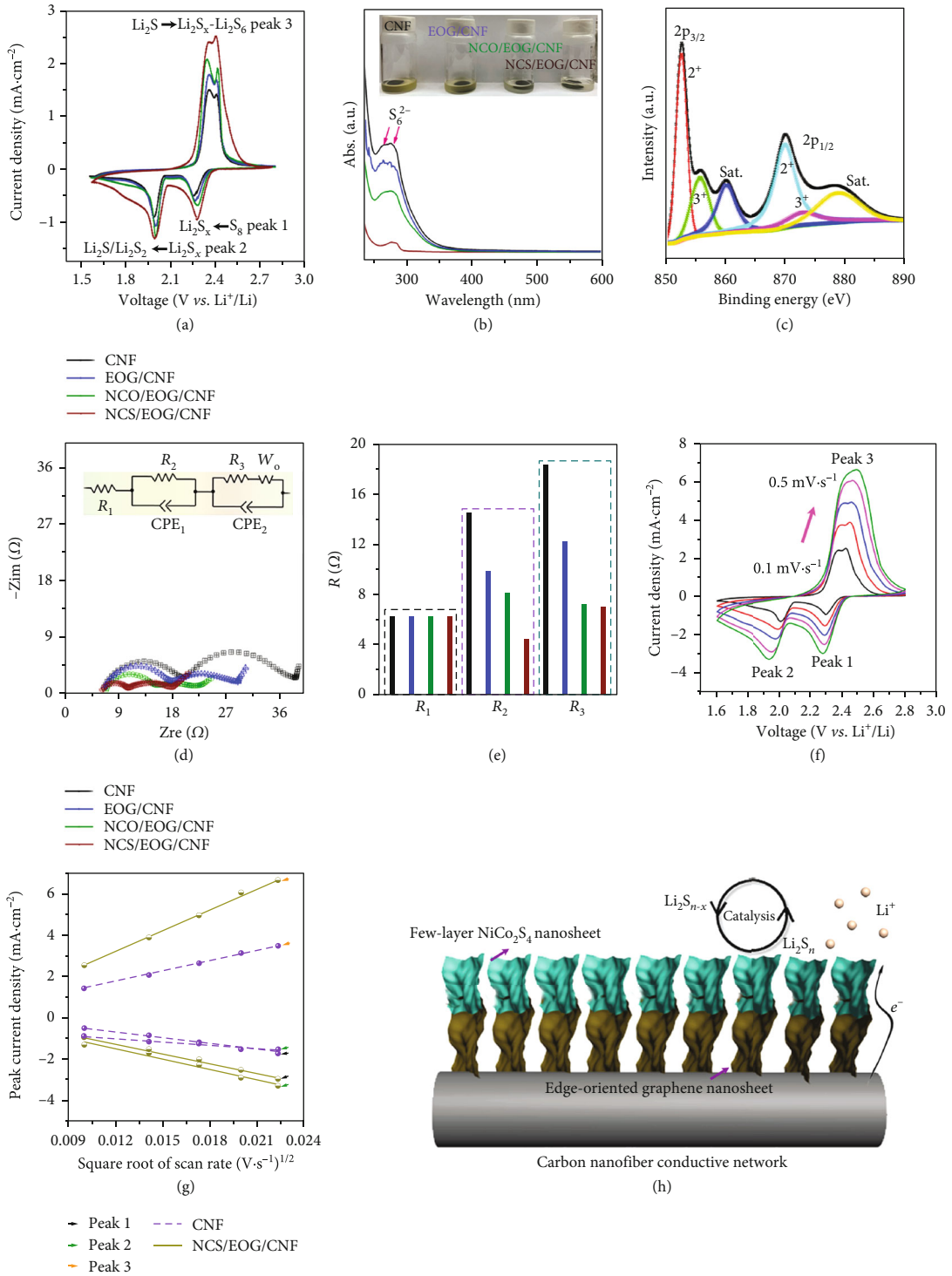

Figure 2: (a) CV curves of LSB cells with different overlayers incorporated in the cathode. (b) UV-Vis absorption spectra of Li_2S_6 solution after being soaked with different layers (inset is the photograph showing the solution color difference after soaking). (c) High-resolution XPS spectrum of Ni 2p of NCS after Li_2S_6 absorption. (d) EIS Nyquist plots of fresh cells with different overlayers incorporated in the cathode (sulfur loading: 2 mg·cm^{-2}; inset: the equivalent circuit for modeling). (e) The derived three resistance values in the equivalent circuit of (d). (f) CV curves recorded on the NCS/EOG/CNF cell under different scan rates. (g) The plots of peak current density versus square root of the scan rate for the redox reactions. (h) Schematic illustration of the function of NCS/EOG/CNF catalytic overlayer in accelerating LiPSs conversion processes.

For every redox peak, the cell with the NCS/EOG/CNF overlayer shows a much higher value than that without an overlayer, revealing the crucial roles of the NCS/EOG/CNF overlayer in catalytically expediting the reaction kinetics. With the strong interaction between LiPSs and the catalytic sites in the catalytic layer, the activation energy can be largely decreased during the redox reactions, leading to fast LiPSs conversion processes [3, 9] and thus accelerated Li^+ flux to the electrode. It also has been noted that the catalytic sites could also enhance even Li^+ flux which will result in uniform deposition of S_8 or Li_2S_2/Li_2S nanoparticles [49], further facilitating the redox reactions by the shortened diffusion distance in these nanoparticles.

The impressive electrocatalytic performance of a thin NCS/EOG/CNF overlayer in the cathode can be attributed to two major merits of the unique structure design, as schematically illustrated in Figure 2(h): (1) EOG/CNF provides a highly conductive scaffold (the resistance of the EOG/CNF film decreases to 2.8 Ω from the value of 20.3 Ω recorded on the CNF film) and serves as a structural template with plenty of surface areas for NCO and NCS to grow onto, which not only guarantees the high electron transport ability but also templatizes the metal oxide/sulfide thin sheet growth with vertical orientation. This structure provides high-density and easily accessible active sites and thus dramatically reduces the needed mass of NCS. (2) Transition metal sulfides (TMSs) with highly catalytic activity towards polysulfide conversion have been demonstrated previously; the soft acid-soft base interaction between TM cations and S^{2-}/S_2^{2-} anions results in a high density of valence electrons in TM atoms, which makes these TMSs efficient binding sites for polysulfides [50]. In addition, it has been proved by using density functional theory calculation that the energy barriers for Li_2S decomposition on the TMS surface can be significantly reduced owing to the strong interaction between lithium cations and sulfur anions in TMSs [26]. And this oriented structure reported here can make the edge sites of NCS nanosheets expose to the electrolyte, which may contain more defects and thus are expected to be more active in absorbing the polysulfide species, fully taking advantage of their catalytic capability.

3.3. Li-S Battery Performance of the NCS/EOG/CNF Overlayer. With the best catalytic function exhibited by the NCS/EOG/CNF overlayer, it is not a surprise that the NCS/EOG/CNF cell delivered the highest performance among the several cell configurations. Figure 3(a) presents the potential profiles of these cells at the second charge-discharge cycle at 0.1 C. The plateaus presented in these curves are associated with the polysulfide redox reaction peaks in the CV curves (Figure 2(a)). Obviously, cells with a catalytic overlayer show more broaden plateaus and smaller polarization. For the EOG/CNF cell, the improvement is mostly ascribed to the high conductivity of the EOG/CNF film, which facilitates electron transport and physically blocks the diffusion of polysulfide to the anode side. The active EOG nanoflake edges [51] also catalytically promote the redox process of the sulfur electrode. After growth of NCO or NCS nanosheets along EOG nanoflakes, the surface as well as the edge-determined catalytic functions of oxides and sulfides, with more active sites and better catalytic ability, further efficiently catalyze the polysulfide redox processes [21]. As a result, the Coulombic efficiency reaches 99.7%, 97.2%, and 99.5% for the NCS/EOG/CNF, NCO/EOG/CNF, and EOG/CNF cell, respectively, while it is only 94.2% for the CNF cell without a cathode overlayer. It should be noted here, although metal oxides have polar surfaces to absorb and enhance the redox kinetics of polysulfide species, realize the controllable deposition of Li_2S, and improve the electrochemical performance of Li-S batteries (Figure 3(a)) [3], their counterparts, metal sulfides, usually exhibit better electrical conductivity because of the more covalent nature imparted by soft basic S^{2-}/S_2^{2-} ions instead of the hard basic O^{2-} ion and higher binding energy toward polysulfide [50], resulting in better battery performances consequently. The NCS/EOG/CNF cell after the second fully discharged process was disassembled, and the morphology of the electrode and NCS/EOG/CNF overlayer was further studied by SEM technique. As shown in Figure S16, the carbon nanofibers in CNF maintain their original shape with some nanoparticles attached on their surfaces which are the reserved Li_2S reduction product. For the NCS/EOG/CNF overlayer, the vertical orientation of these nanosheets can still be clearly observed, demonstrating their stability during battery cycling.

Figure 3(b) compares the capacity and the Coulombic efficiency of the four cells (sulfur loading of 2 mg·cm^{-2}) in the first 100 cycles at different current densities. Without the assistance of a catalytic overlayer in the cathode, the cell capacity only reaches ~750 mAh·g^{-1} at 0.1 C and drops significantly as the current density ramps up. At the 100th cycle, its capacity is only 495 mAh·g^{-1} with a Coulombic efficiency of 91.3% at 0.3 C. In contrast, under the same testing condition, the EOG/CNF cell has a capacity of 957 mAh·g^{-1} with 98.2% efficiency, the NCO/EOG/CNF cell has a capacity of 1046 mAh·g^{-1} with 98.3% efficiency, and the NCS/EOG/CNF cell has a capacity of 1072 mAh·g^{-1} with 98.5% efficiency at the 100th cycle. The NCS/CNF cell with 2 mg·cm^{-2} of sulfur loading was also cycled at 0.3 C; in spite of the increased usage amount of the NCS catalyst in the NCS/CNF film, its specific capacity (~950 mAh·g^{-1}, Figure S17) is still lower than that of the NCS/EOG/CNF cell, further demonstrating the effectiveness of the vertical structure in the NCS/EOG/CNF film in promoting the Li-S battery performances. As it is known, the internal shortcut due to LiPSs shuttling between the cathode and the anode is largely responsible for the low Coulombic efficiency of LSB [52, 53]. Incorporation of a thin catalytic overlayer in the cathode dramatically improves the LiPSs conversion kinetics and thus reduces their shuttling, and hence, cells show above 98% Coulombic efficiency, representing a huge leap from the ~91% recorded on the cell without an overlayer in the cathode. Even with a reduced electrolyte/sulfur (E/S) ratio of 10, the NCS-derived cell with 2 mg·cm^{-2} of sulfur loading can still deliver around 900 mAh·g^{-1} of specific capacity at 0.3 C, with Coulombic efficiency ~98% (Figure S18). The voltage profile evolution of the NCS/EOG/CNF cell at different cycle numbers is extracted and summarized in

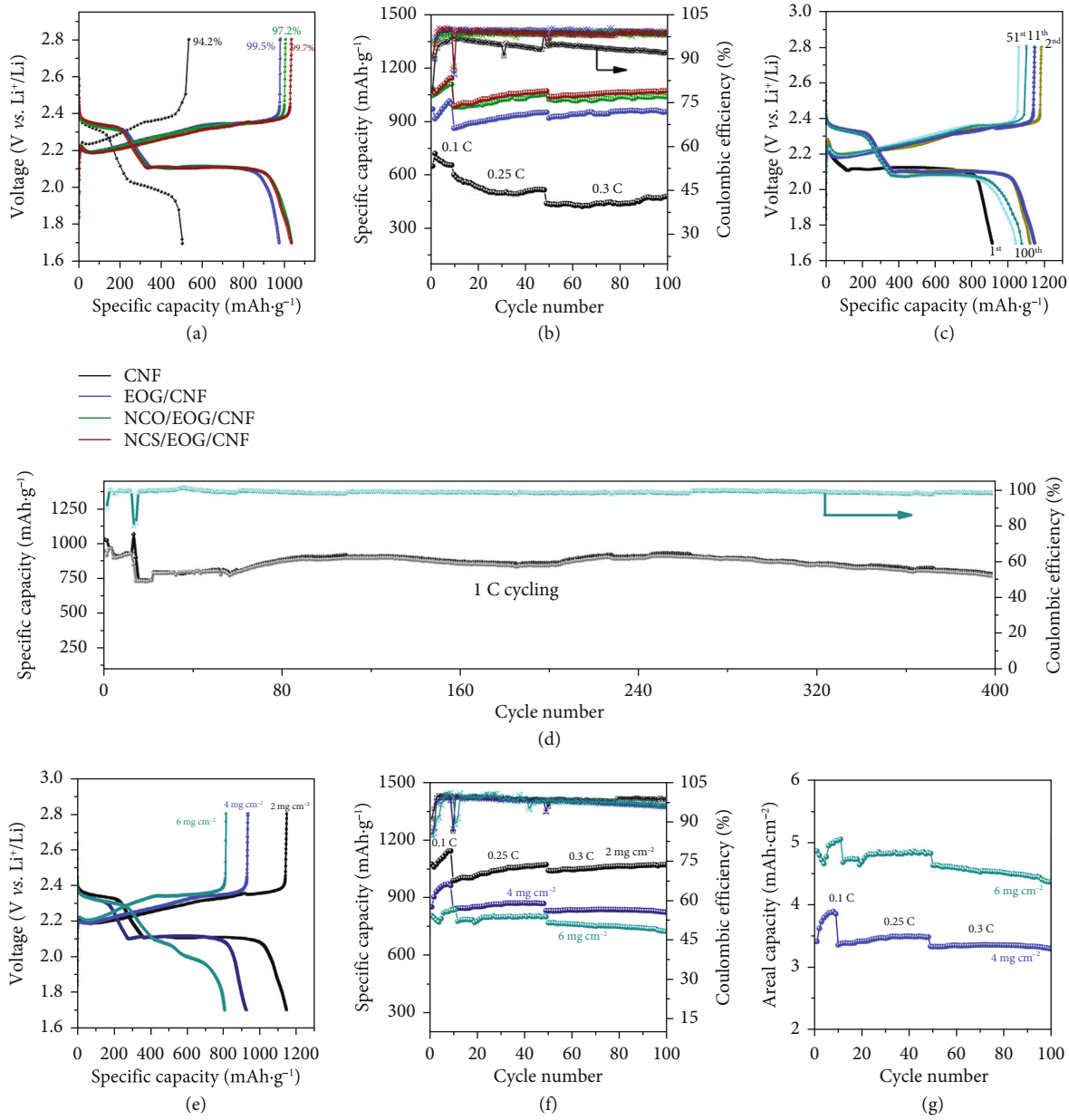

Figure 3: (a) The voltage profiles in the 2nd charge-discharge cycle and (b) cycling performance at the rate of 0.1 C–0.3 C of LSBs with different overlayers incorporated in the cathode. (c) Charge-discharge voltage profiles in different cycles for the NCS/EOG/CNF cell. (d) Long-term cycling performance of the NCS/EOG/CNF cell at 1 C. (e) Charge-discharge curves in the 2nd cycle and (f, g) cycling performance of NCS/EOG/CNF cells with different sulfur loadings of 2, 4, and 6 mg·cm^{-2}.

Figure 3(c). With the current density increasing from 0.1 C to 0.3 C, the plateaus of the redox reactions keep being stable, suggesting the good conductivity and catalytic activity of the overlayer-incorporated cathode.

With diminished LiPSs shuttling and the related effects, the NCS/EOG/CNF catalytic overlayer significantly improves the performance stability of LSB cells. As shown in Figure 3(d), an NCS/EOG/CNF cell with a sulfur load of 2 mg·cm^{-2} was cycled at 1 C for 400 cycles (the first ten cycles were recorded at 0.1 C for stabilizing purposes). Although the capacity drops from 1100 to 750 mAh·g^{-1} when the charge-discharge rate is suddenly switched from 0.1 C to 1 C, it slowly recovers to 930 mAh·g^{-1} upon cycling. At the 400th cycle, the cell retains a capacity of 740 mAh·g^{-1} at 1 C, which is in the top tier of performance in comparison with other metal oxide- and sulfide catalyst-based LSBs [21]. As shown in Figure S19, the NCS/EOG/CNF-functionalized cell showed impressive rate capability and could deliver 480 mAh·g^{-1} at a very high rate of 3 C. Their Coulombic efficiency was generally above 98% except when the rate was suddenly changed.

We also prepared cathodes with different sulfur loadings and their performances are presented in Figures 3(e)–3(g). The specific capacity of each cell at the 2nd cycle (Figure 3(e)) is around 1150, 989, and 800 mAh·g^{-1} for sulfur loading of 2, 4, and 6 mg·cm^{-2}, respectively. In comparison

with that of the NCS/EOG/CNF cells with low sulfur loadings, the voltage profile of the cell with 6 mg·cm^{-2} of sulfur loading shows shortened and distorted charge and discharge plateaus. This phenomenon is considered to be caused by the aggregation of the nonconductive sulfur and Li_2S species which can retard the electrochemical kinetics of electrode reactions (such as poor electron and ion transportation processes) and exacerbate the polysulfide shuttling process. In addition, due to the high sulfur loading, the required high areal charge-discharge current density will also cause high polarization in the cathode during cycling. By cycling these cells for 100 cycles, all of them demonstrate stable capacity retention, with Coulombic efficiency maintaining above 98%. For the areal capacity, the cell with 6 mg·cm^{-2} sulfur loading can reach to 4.5 mAh·cm^{-2} at the 100th cycle at 0.3 C. Figure S20 compares the areal capacity achieved in this work with those reporting Li-S electrode/interlayer studies [44, 54–59].

Besides the sulfur mass loading, the sulfur fraction in the cathode is another important criterion to evaluate the specific energy of the total cathode, including the current collector. In the conventional sulfur cathode design that uses a sulfur paste coated on a typical 15 μm thick Al foil current collector, even if we assume a high sulfur fraction (70% in the paste) and high sulfur mass loading (6 mg·cm^{-2}), both being rare cases ever reported in the literature, when the mass of the Al foil (4.05 mg·cm^{-2}) is included, the sulfur fraction becomes only 47.5% in the whole cathode. In our freestanding cathode structure design, the total mass density of CNF and NCS/EOG/CNF layers is 3.12 mg·cm^{-2}, so the sulfur fraction in the whole cathode reaches 65.8% for 6 mg·cm^{-2} sulfur loading. This gives a sulfur fraction increase by 38.5% over the conventional design. Correspondingly, the specific energy based on the total cathode mass will be translated into 38.5% increase. It is noted that the introduction of the overlayer can also contribute to build a uniform current distribution across the electrode, helping restricting the growth of lithium dendrites upon long-term cycling operation [60].

4. Conclusions

In this work, few-layer NCS nanosheets were successfully grown on a vertical graphene-modified CNF film, which was incorporated into the sulfur cathode design for LSBs. With its edge-oriented structure and fully exposed and easily accessed surface area, the catalytic activity of NCS towards polysulfide absorption/conversion can be fully exerted even with a small loading. In addition, the flexible EOG/CNF substrate can also significantly enhance the electron conductivity of the overlayer and physically shield the polysulfides from diffusing to the anode side. As a result, LSBs with a thin NCS/EOG/CNF overlayer give much better battery performances in terms of specific capacity, over potential, rate ability, and cycling stability than the one without an overlayer design. It is expected that such a novel structure design and the corresponding synthesis strategy could also be applied in constructing other catalytic material-based nanostructures for broad applications, such as fuel cells, electrochemical hydrogen production, and electrochemical CO_2 reduction.

Data Availability

All data needed to evaluate the conclusions in the paper are present in the paper and/or the Supplementary Materials. Additional data related to this paper may be requested from the corresponding author (Zhaoyang Fan, Zhaoyang.Fan@asu.edu).

Conflicts of Interest

The authors declare that there is no conflict of interest regarding the publication of this article.

Acknowledgments

This work was supported by the National Science Foundation of USA (1931737).

Supplementary Materials

SEM and TEM images of different NCO/EOG/CNF and NCS/EOG/CNF samples, XPS spectra of EOG/CNF and NCS/EOG/CNF samples, CV curves for CNF and NCS/EOG/CNF-based cells, cycling performance of NCS/CNF based cell, Rate capability cycling performance of the NCS/EOG/CNF based cell, Figure of comparison of the areal capacity achieved in this work with those reporting electrode/interlayer studies. *(Supplementary Materials)*

References

[1] Y. X. Yin, S. Xin, Y. G. Guo, and L. J. Wan, "Lithium-sulfur batteries: electrochemistry, materials, and prospects," *Angewandte Chemie International Edition*, vol. 52, no. 50, pp. 13186–13200, 2013.

[2] W. M. Kang, N. P. Deng, J. G. Ju et al., "A review of recent developments in rechargeable lithium-sulfur batteries," *Nanoscale*, vol. 8, no. 37, pp. 16541–16588, 2016.

[3] X. Y. Tao, J. G. Wang, C. Liu et al., "Balancing surface adsorption and diffusion of lithium-polysulfides on nonconductive oxides for lithium-sulfur battery design," *Nature Communications*, vol. 7, p. 9, 2016.

[4] S. Li, D. Leng, W. Li et al., "Recent progress in developing Li_2S cathodes for Li-S batteries," *Energy Storage Materials*, vol. 27, pp. 279–296, 2020.

[5] X. Liang, C. Hart, Q. Pang, A. Garsuch, T. Weiss, and L. F. Nazar, "A highly efficient polysulfide mediator for lithium-sulfur batteries," *Nature Communications*, vol. 6, p. 8, 2015.

[6] N. Jayaprakash, J. Shen, S. S. Moganty, A. Corona, and L. A. Archer, "Porous hollow carbon@ sulfur composites for high-power lithium–sulfur batteries," *Angewandte Chemie International Edition*, vol. 50, no. 26, pp. 5904–5908, 2011.

[7] A. Manthiram, S. H. Chung, and C. X. Zu, "Lithium-sulfur batteries: progress and prospects," *Advanced Materials*, vol. 27, no. 12, pp. 1980–2006, 2015.

[8] S. Q. Li, T. Mou, G. F. Ren et al., "Gel based sulfur cathodes with a high sulfur content and large mass loading for high-

performance lithium-sulfur batteries," *Journal of Materials Chemistry A*, vol. 5, no. 4, pp. 1650–1657, 2017.

[9] J. R. He and A. Manthiram, "A review on the status and challenges of electrocatalysts in lithium-sulfur batteries," *Energy Storage Materials*, vol. 20, pp. 55–70, 2019.

[10] H. Chen, M. Ling, L. Hencz et al., "Exploring chemical, mechanical, and electrical functionalities of binders for advanced energy-storage devices," *Chemical Reviews*, vol. 118, no. 18, pp. 8936–8982, 2018.

[11] C. Chen, Q. B. Jiang, H. F. Xu et al., "Ni/SiO_2/graphene-modified separator as a multifunctional polysulfide barrier for advanced lithium-sulfur batteries," *Nano Energy*, vol. 76, p. 8, 2020.

[12] W. Chen, T. Y. Lei, C. Y. Wu et al., "Designing safe electrolyte systems for a high-stability lithium-sulfur battery," *Advanced Energy Materials*, vol. 8, no. 10, p. 24, 2018.

[13] S. P. Wu, R. Y. Ge, M. J. Lu, R. Xu, and Z. Zhang, "Graphene-based nano-materials for lithium-sulfur battery and sodium-ion battery," *Nano Energy*, vol. 15, pp. 379–405, 2015.

[14] J. C. Guo, Y. H. Xu, and C. S. Wang, "Sulfur-impregnated disordered carbon nanotubes cathode for lithium-sulfur batteries," *Nano Letters*, vol. 11, no. 10, pp. 4288–4294, 2011.

[15] N. Brun, K. Sakaushi, L. H. Yu, L. Giebeler, J. Eckert, and M. M. Titirici, "Hydrothermal carbon-based nanostructured hollow spheres as electrode materials for high-power lithium-sulfur batteries," *Physical Chemistry Chemical Physics*, vol. 15, no. 16, pp. 6080–6087, 2013.

[16] L. H. Zhang, B. He, W. C. Li, and A. H. Lu, "Surface free energy-induced assembly to the synthesis of grid-like multi-cavity carbon spheres with high level in-cavity encapsulation for lithium-sulfur cathode," *Advanced Energy Materials*, vol. 7, no. 22, article 1701518, p. 7, 2017.

[17] Z. Li, J. T. Zhang, B. Y. Guan, D. Wang, L. M. Liu, and X. W. Lou, "A sulfur host based on titanium monoxide@carbon hollow spheres for advanced lithium-sulfur batteries," *Nature Communications*, vol. 7, p. 11, 2016.

[18] Y. Y. Peng, Y. Y. Zhang, J. X. Huang et al., "Nitrogen and oxygen dual-doped hollow carbon nanospheres derived from catechol/polyamine as sulfur hosts for advanced lithium sulfur batteries," *Carbon*, vol. 124, pp. 23–33, 2017.

[19] A. Schneider, C. Suchomski, H. Sommer, J. Janek, and T. Brezesinski, "Free-standing and binder-free highly N-doped carbon/sulfur cathodes with tailorable loading for high-areal-capacity lithium-sulfur batteries," *Journal of Materials Chemistry A*, vol. 3, no. 41, pp. 20482–20486, 2015.

[20] Y. Yang, G. H. Yu, J. J. Cha et al., "Improving the performance of lithium-sulfur batteries by conductive polymer coating," *ACS Nano*, vol. 5, no. 11, pp. 9187–9193, 2011.

[21] X. Liu, J. Q. Huang, Q. Zhang, and L. Q. Mai, "Nanostructured metal oxides and sulfides for lithium-sulfur batteries," *Advanced Materials*, vol. 29, no. 20, article 1601759, p. 25, 2017.

[22] S. Rehman, T. Y. Tang, Z. Ali, X. X. Huang, and Y. L. Hou, "Integrated design of MnO2@carbon hollow nanoboxes to synergistically encapsulate polysulfides for empowering lithium sulfur batteries," *Small*, vol. 13, no. 20, article 1700087, p. 8, 2017.

[23] S. Majumder, M. H. Shao, Y. F. Deng, and G. H. Chen, "Ultrathin sheets of MoS_2/g-C_3N_4 composite as a good hosting material of sulfur for lithium-sulfur batteries," *Journal of Power Sources*, vol. 431, pp. 93–104, 2019.

[24] L. Tan, X. H. Li, Z. X. Wang, H. J. Guo, and J. X. Wang, "Lightweight reduced graphene oxide@MoS2 interlayer as polysulfide barrier for high-performance lithium-sulfur batteries," *ACS Applied Materials & Interfaces*, vol. 10, no. 4, pp. 3707–3713, 2018.

[25] J. Wang, L. Jia, J. Zhong et al., "Single-atom catalyst boosts electrochemical conversion reactions in batteries," *Energy Storage Materials*, vol. 18, pp. 246–252, 2019.

[26] G. M. Zhou, H. Z. Tian, Y. Jin et al., "Catalytic oxidation of Li2S on the surface of metal sulfides for Li-S batteries," *Proceedings of the National Academy of Sciences of the United States of America*, vol. 114, no. 5, pp. 840–845, 2017.

[27] N. Wei, J. S. Cai, R. C. Wang et al., "Elevated polysulfide regulation by an ultralight all-CVD-built ReS2@N-doped graphene heterostructure interlayer for lithium-sulfur batteries," *Nano Energy*, vol. 66, article 104190, p. 8, 2019.

[28] J. He, Y. Chen, and A. Manthiram, "MOF-derived Cobalt Sulfide Grown on 3D Graphene Foam as an Efficient Sulfur Host for Long-Life Lithium-Sulfur Batteries," *iScience*, vol. 4, pp. 36–43, 2018.

[29] W. Y. Li, N. Islam, S. Azam, Z. Xu, J. Warzywoda, and Z. Y. Fan, "ZIF-67-derived edge-oriented graphene clusters coupled with carbon nanotubes containing encapsulated co nanoparticles for high-frequency electrochemical capacitors," *Sustainable Energy & Fuels*, vol. 3, no. 11, pp. 3029–3037, 2019.

[30] J. R. Miller, R. A. Outlaw, and B. C. Holloway, "Graphene double-layer capacitor with ac line-filtering performance," *Science*, vol. 329, no. 5999, pp. 1637–1639, 2010.

[31] G. Ren, M. N. F. Hoque, X. Pan, J. Warzywoda, and Z. Fan, "Vertically aligned VO 2 (B) nanobelt forest and its three-dimensional structure on oriented graphene for energy storage," *Journal of Materials Chemistry A*, vol. 3, no. 20, pp. 10787–10794, 2015.

[32] Y. Fan, Z. Yang, W. X. Hua et al., "Functionalized boron nitride nanosheets/graphene interlayer for fast and long-life lithium-sulfur batteries," *Advanced Energy Materials*, vol. 7, no. 13, article 1602380, Article ID 10.1002/aenm.201602380, p. 6, 2017.

[33] X. F. Wang, Z. X. Wang, and L. Q. Chen, "Reduced graphene oxide film as a shuttle-inhibiting interlayer in a lithium- sulfur battery," *Journal of Power Sources*, vol. 242, pp. 65–69, 2013.

[34] L. L. Fan, M. Li, X. F. Li, W. Xiao, Z. W. Chen, and J. Lu, "Interlayer material selection for lithium-sulfur batteries," *Joule*, vol. 3, no. 2, pp. 361–386, 2019.

[35] S. Li, G. Ren, M. N. F. Hoque, Z. Dong, J. Warzywoda, and Z. Fan, "Carbonized cellulose paper as an effective interlayer in lithium-sulfur batteries," *Applied Surface Science*, vol. 396, pp. 637–643, 2017.

[36] G. X. Wang, X. P. Shen, J. Yao, and J. Park, "Graphene nanosheets for enhanced lithium storage in lithium ion batteries," *Carbon*, vol. 47, no. 8, pp. 2049–2053, 2009.

[37] J. F. Liu, D. Takeshi, D. Orejon, K. Sasaki, and S. M. Lyth, "Defective nitrogen-doped graphene foam: a metal-free, non-precious electrocatalyst for the oxygen reduction reaction in acid," *Journal of the Electrochemical Society*, vol. 161, no. 4, pp. F544–F550, 2014.

[38] Y. J. Chen, J. Zhu, B. H. Qu, B. A. Lu, and Z. Xu, "Graphene improving lithium-ion battery performance by construction

of $NiCo_2O_4$/graphene hybrid nanosheet arrays," *Nano Energy*, vol. 3, pp. 88–94, 2014.

[39] L. F. Shen, J. Wang, G. Y. Xu, H. S. Li, H. Dou, and X. G. Zhang, "$NiCo_2S_4$ nanosheets grown on nitrogen-doped carbon foams as an advanced electrode for supercapacitors," *Advanced Energy Materials*, vol. 5, no. 3, article 1400977, p. 7, 2015.

[40] H. C. Chen, S. Chen, H. Y. Shao et al., "Hierarchical $NiCo_2S_4$ nanotube@$NiCo_2S_4$ nanosheet arrays on Ni foam for high-performance supercapacitors," *Chemistry - An Asian Journal*, vol. 11, no. 2, pp. 248–255, 2016.

[41] M. Zhao, H. J. Peng, Z. W. Zhang et al., "Activating inert metallic compounds for high-rate lithium -sulfur batteries through in situ etching of extrinsic metal," *Angewandte Chemie International Edition*, vol. 58, no. 12, pp. 3779–3783, 2019.

[42] Y. K. Yi, H. P. Li, H. H. Chang et al., "Few-layer boron nitride with engineered nitrogen vacancies for promoting conversion of polysulfide as a cathode matrix for lithium-sulfur batteries," *Chemistry – A European Journal*, vol. 25, no. 34, pp. 8112–8117, 2019.

[43] X. Huang, Z. L. Wang, R. Knibbe et al., "Cyclic voltammetry in lithium-sulfur batteries-challenges and opportunities," *Energy Technology*, vol. 7, no. 8, p. 13, 2019.

[44] H. J. Peng, Z. W. Zhang, J. Q. Huang et al., "A cooperative interface for highly efficient lithium–sulfur batteries," *Advanced Materials*, vol. 28, no. 43, pp. 9551–9558, 2016.

[45] S. Li, P. Xu, M. K. Aslam et al., "Propelling polysulfide conversion for high-loading lithium-sulfur batteries through highly sulfiphilic $NiCo_2S_4$ nanotubes," *Energy Storage Materials*, vol. 27, pp. 51–60, 2020.

[46] Z. F. Deng, Z. A. Zhang, Y. Q. Lai, J. Liu, J. Li, and Y. X. Liu, "Electrochemical impedance spectroscopy study of a lithium/sulfur battery: modeling and analysis of capacity fading," *Journal of the Electrochemical Society*, vol. 160, no. 4, pp. A553–A558, 2013.

[47] V. S. Kolosnitsyn, E. V. Kuzmina, E. V. Karaseva, and S. E. Mochalov, "A study of the electrochemical processes in lithium-sulphur cells by impedance spectroscopy," *Journal of Power Sources*, vol. 196, no. 3, pp. 1478–1482, 2011.

[48] Y. T. Liu, D. D. Han, L. Wang, G. R. Li, S. Liu, and X. P. Gao, "$NiCo_2O_4$ nanofibers as carbon-free sulfur immobilizer to fabricate sulfur-based composite with high volumetric capacity for lithium-sulfur battery," *Advanced Energy Materials*, vol. 9, no. 11, article 1803477, p. 10, 2019.

[49] Y. F. Luo, N. N. Luo, W. B. Kong et al., "Multifunctional interlayer based on molybdenum diphosphide catalyst and carbon nanotube film for lithium-sulfur batteries," *Small*, vol. 14, no. 8, p. 9, 2018.

[50] X. Chen, H. J. Peng, R. Zhang et al., "An analogous periodic law for strong anchoring of polysulfides on polar hosts in lithium sulfur batteries: S- or Li-binding on first-row transition-metal sulfides?," *ACS Energy Letters*, vol. 2, no. 4, pp. 795–801, 2017.

[51] X. Pan, K. Zhu, G. Ren, N. Islam, J. Warzywoda, and Z. Fan, "Electrocatalytic properties of a vertically oriented graphene film and its application as a catalytic counter electrode for dye-sensitized solar cells," *Journal of Materials Chemistry A*, vol. 2, no. 32, pp. 12746–12753, 2014.

[52] I. Bauer, S. Thieme, J. Bruckner, H. Althues, and S. Kaskel, "Reduced polysulfide shuttle in lithium-sulfur batteries using Nafion-based separators," *Journal of Power Sources*, vol. 251, pp. 417–422, 2014.

[53] X. B. Cheng, J. Q. Huang, H. J. Peng et al., "Polysulfide shuttle control: towards a lithium-sulfur battery with superior capacity performance up to 1000 cycles by matching the sulfur/electrolyte loading," *Journal of Power Sources*, vol. 253, pp. 263–268, 2014.

[54] L. Jiao, C. Zhang, C. N. Geng et al., "Capture and catalytic conversion of polysulfides by in situ built TiO2-MXene heterostructures for lithium-sulfur batteries," *Advanced Energy Materials*, vol. 9, no. 19, article 1900219, p. 9, 2019.

[55] Q. C. Li, Y. Z. Song, R. Z. Xu et al., "Biotemplating growth of nepenthes-like N-doped graphene as a bifunctional polysulfide scavenger for Li-S batteries," *ACS Nano*, vol. 12, no. 10, pp. 10240–10250, 2018.

[56] Y. J. Li, W. Y. Wang, X. X. Liu et al., "Engineering stable electrode-separator interfaces with ultrathin conductive polymer layer for high-energy-density Li-S batteries," *Energy Storage Materials*, vol. 23, pp. 261–268, 2019.

[57] F. Pei, L. L. Lin, A. Fu et al., "A two-dimensional porous carbon-modified separator for high-energy-density Li-S batteries," *Joule*, vol. 2, no. 2, pp. 323–336, 2018.

[58] Y. Z. Song, S. Y. Zhao, Y. R. Chen et al., "Enhanced sulfur redox and polysulfide regulation via porous VN-modified separator for Li-S batteries," *ACS Applied Materials & Interfaces*, vol. 11, no. 6, pp. 5687–5694, 2019.

[59] J. Liu, D. G. D. Galpaya, L. J. Yan et al., "Exploiting a robust biopolymer network binder for an ultrahigh-areal-capacity Li-S battery," *Energy & Environmental Science*, vol. 10, no. 3, pp. 750–755, 2017.

[60] J. Q. Huang, Q. Zhang, and F. Wei, "Multi-functional separator/interlayer system for high-stable lithium-sulfur batteries: progress and prospects," *Energy Storage Materials*, vol. 1, pp. 127–145, 2015.